

Cover Page



Universiteit Leiden



The handle <http://hdl.handle.net/1887/53199> holds various files of this Leiden University dissertation.

**Author:** Zuiden, B.C. van

**Title:** Topology and geometry in chiral liquids

**Issue Date:** 2017-09-27

## Chapter 3.

# Chiral active liquids with self-rotation



**T**HE LAST TWO DECADES have seen significant progress in our understanding of active matter. Early theoretical progress [33, 52, 69] has been accompanied by the engineering of soft materials made of self-propelled polymers, colloids, emulsions, and grains [11, 43, 56, 59, 76, 79, 84, 85], which exhibit novel nonequilibrium phenomena. Prominent examples include phase separation of repulsive spheres, giant number fluctuations away from criticality, and long-range orientational order in two-dimensional flocks [27, 110, 148].

The systems mentioned above share the characteristic that constituents acquire translational momentum due to active propulsion, but rotate only in response to collisions or diffusion. By contrast, insights into the consequences of active *rotation* without self-propulsion remain scarce, even though this situation is relevant to a wide range of experimental systems [6] including spinning microorganisms [21, 91], treadmilling proteins [2], sperm cell and microtubule aggregates [67, 108], shaken chiral grains [111], light-powered chiral colloids [23], thermally and chemically powered liquid crystals [17, 123], electrorheological fluids [98], and biological and synthetic cilia driven by rotary molecular motors [47].

Until now, theoretical and numerical studies on ensembles of active spinners have separately addressed their phase dynamics and their spatial organization. The emergence and robustness of synchronized rotation in lattices of hydrodynamically-coupled rotors [87, 88] has been studied as an archetype of Kuramoto dynamics in coupled oscillator systems [105]. In these models the lattice geometry is imposed, a situation relevant, for instance, to

the propagation of metachronal waves at the surface of ciliated tissues [10, 64, 81, 127]. Local orientational synchronization has also been observed in self-organized disordered arrays of rotating rods [48, 107]. A separate class of numerical studies has been devoted to the *spatial structures* of ensembles of active spinners interacting either via contact or hydrodynamic interactions [1, 12, 22, 24, 32, 41, 120]. Special attention has been paid to phase separation in binary mixtures of counterrotating spinners and to hydrodynamic interactions yielding spatial ordering.

Here, we bridge the gap between these two lines of research. Combining numerical simulations and analytical theory we demonstrate the inherent interplay between the spatial structure and the phase dynamics of active spinners. We uncover a generic competition between monopole-like interactions that dominate at large separations, and shorter-range multipole gear-like interactions. We find that their interplay frustrates ordered states but also yields novel spatiotemporal order and unanticipated collective flows including edge currents.

We study a prototypical system of soft dimers interacting via repulsive interactions and undergoing unidirectional active rotation as sketched in fig. 3.1. When isolated, dimers spin in response to the active torque, attaining a steady-state spinning speed due to background friction. As they get closer, the multipole character of the pair interactions resists the rotation of adjacent dimers, fig. 3.1 b–c. At very high densities, the relative motion of neighbours is completely obstructed, fig. 3.1 d. By tuning the density, we explore how the frustration between monopole and multipole interactions plays out as their relative strengths are varied. We observe transitions from collections of independently spinning dimers to unusual crystal states which are ordered in particle position as well as orientation over time, to active spinner liquids, to jammed states. Repulsive interactions with boundaries also obstruct spinning fig. 3.1 e; to compensate, the system channels the rotational drive into linear momentum, giving rise to robust edge currents and collective motion.

Our model system consists of a two-dimensional ensemble of  $N$  like-charge dimers, each consisting of two point particles of mass  $m$  connected by a stiff link of length  $d$ , fig. 3.1 a. Point particles interact only via a repulsive pair potential of the Yukawa form  $b e^{-\kappa r} / r$ , where  $b$  sets the overall strength of the repulsion,  $r$  is the inter-particle separation distance, and  $\kappa$  is the inverse screening length, see fig. 3.1. By setting  $\kappa^{-1} \sim d$ , we discourage dimer links from crossing each other and also maximize the orientational dependence of the effective pair interaction between dimers.

Each dimer is actively driven implemented by a torque  $\tau = Fd$  implemented as a force dipole, fig. 3.1 a. Energy is dissipated by drag forces acting on each particle with associated drag coefficient  $\gamma$ . The equations of motion for the position,  $\mathbf{r}_i$  and orientation  $\theta_i$  of the  $i^{\text{th}}$  dimer are

$$2m\ddot{\mathbf{r}}_i = -2\gamma\dot{\mathbf{r}}_i - \partial_{\mathbf{r}_i} \sum_{j \neq i} V(\mathbf{r}_j - \mathbf{r}_i, \theta_i, \theta_j), \quad (3.1)$$

$$I\ddot{\theta}_i = \tau - \gamma_\Omega\dot{\theta}_i - \partial_{\theta_i} \sum_{j \neq i} \mathcal{V}(\mathbf{r}_j - \mathbf{r}_i, \theta_i, \theta_j), \quad (3.2)$$

where  $I = \frac{1}{2}md^2$  and  $\gamma_\Omega = \frac{1}{2}\gamma d^2$  are the moment of inertia and rotational friction coefficients respectively, and the position- and orientation-dependent interaction potentials  $V$  and  $\mathcal{V}$  are derived from the Yukawa pair interactions between the point particles. An isolated dimer attains a steady state of counter-clockwise rotation about its center with a constant spinning speed  $\Omega_0 = \tau/\gamma_\Omega$ , see fig. 3.1 b. We emphasize, however, that the instantaneous orientation of the dimer is *not* dictated by the drive, in contrast to systems where the dimer orientation is slaved to an external field, e.g. colloids driven by a rotating magnetic field [30, 70].

Upon rescaling distances by  $\kappa^{-1}$  and time by  $\Omega_0^{-1}$ , the dynamical equations are characterized by three dimensionless quantities:  $\kappa d$ ,  $\alpha \equiv I\tau/\gamma_\Omega^2$  which measures the characteristic dissipation time for angular momentum in units of the spinning period, and  $\beta^{-1} \equiv \tau/\kappa b$  which quantifies the drive in units of the characteristic interaction energy scale. We focus here on the competition between rotational drive and interactions as the dimer *density* is varied for fixed  $\alpha$  and  $\beta$ , as sketched in fig. 3.1 b–d. We constrain ourselves to the asymptotic limit where both  $\alpha \gg 1$  and  $\beta \gg 1$ .

### 3.1 Systems of Active Spinners

In order to study systems of active interacting spinners, we conducted molecular dynamic simulations for eqs. (3.1) and (3.2). First, we characterized the bulk behavior of systems of active interacting spinners through simulations under periodic boundary conditions in which the dimer density was varied by changing the dimensions of the simulation box with constant screening parameter  $\kappa = 0.725/d$ , particle number  $N = 768$ , and activity parameters

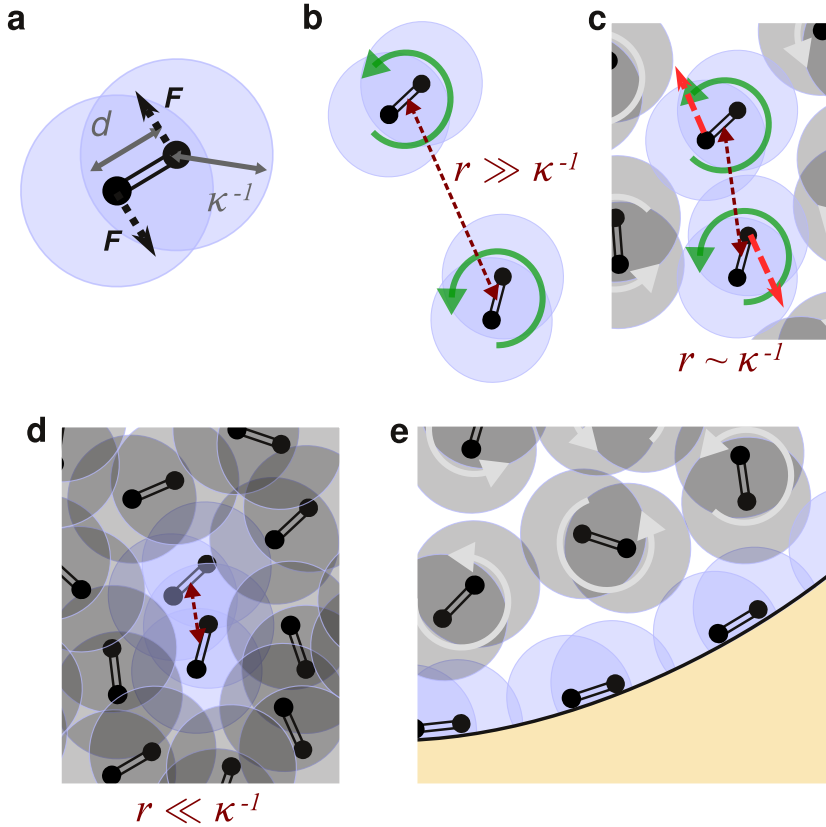


**Figure 3.1: Competing rotation and interactions in active spinners.** **a**, Make-up of a single self-spinning dimer, consisting of a pair of identically-charged particles (black dots), connected by a rigid rod of length  $d$  (double line). Particles repel each other with a Yukawa interaction with screening length  $\kappa^{-1}$  which determines the soft exclusion zone (light blue discs), beyond which the repulsion falls off exponentially with distance. Each particle experiences a force of magnitude  $F$  and direction indicated by dotted arrows, oriented to provide zero net force and a net torque  $\tau = Fd$  on the dimer at all times. **b–d**, The density determines the influence of interactions on dimer dynamics. At large separations (**b**), interactions are negligible and dimers freely rotate at the terminal angular velocity set by the activity and the background drag. As separations become comparable to the screening length (**c**), adjacent dimers still rotate past each other but experience interaction forces (red dashed arrows show instantaneous force due to the interaction between two of the particles) that depend on their instantaneous orientations. At very high densities (**d**), interactions completely obstruct dimer rotation. **e**, Hard boundaries also obstruct dimer rotation, and their effect is transmitted into interior dimers by interactions.

$\alpha = 131$  and  $\beta = 133$ . Second, we characterized the behavior of bulk *and* edge of systems of active interacting spinners by confining such a system in a circular or slab-like geometry while we varied the density — similarly to the method used when characterizing the bulk behavior.

### 3.1.1 Phase behavior

We characterized the bulk behavior of interacting spinners through simulations under periodic boundary conditions in which the dimer density was varied by changing the dimensions of the simulation box with constant screening parameter  $\kappa = 0.725/d$ , particle number  $N = 768$ , and activity parameters  $\alpha = 131$  and  $\beta = 133$ . Density is quantified by the packing fraction  $\phi = A\rho$ , where  $\rho$  is the number density of dimers and  $A = \pi(d + 2\kappa^{-1})^2/4$  is the soft excluded area of a spinning dimer on time scales  $t \gg 1/\Omega_0$ . Figure 3.2 characterises the phase behavior of our system via changes in particle ordering, orientational ordering and dynamics in the nonequilibrium steady states reached at long times. Nearly identical behavior is observed for simulations with  $N = 3072$ , indicating that finite-size effects are negligible.

### 3.1.2 Active spinner crystals

At low packing fractions, the dimers self-organize into a hexagonal crystalline pattern, with little or no change in position, as shown for two representative densities in the first two panels of fig. 3.2 a. In this regime, the repulsions between dimers give rise to a Wigner-like crystal, quantified by high values of the bond-orientational order parameter  $|\langle\psi_6\rangle|$  fig. 3.2 d [triangles]. Although the dimers are highly restricted in their position, they continue to spin without hindrance, attaining the same angular speed as an isolated dimer ( $\langle\dot{\theta}\rangle \equiv \Omega \approx \Omega_0$ , fig. 3.2 e). Apart from small fluctuations, the orientation of dimer  $i$  at time  $t$  has the form  $\theta_i(t) = \Omega_0 t + \delta_i$  with the angular phase  $\delta_i$  defined up to a global phase shift. This state is reminiscent of plastic crystals, but with the equilibrium fluctuations of the orientational degrees of freedom replaced by active rotation: we term this state an *active spinner crystal*.

The crystals display ordering not only in dimer positions, but also in dimer orientations which are phase-locked into regular spatial patterns. The angular phases  $\delta_i$  take on a few discrete values determined by the lattice position. We find evidence for two distinct configurations. At low densities,  $\delta_i$  acquires one of three values  $\{0, \pi/3, 2\pi/3\}$ , with no two neighbors sharing the same value fig. 3.2 c [first panel]. This pattern is identical to the equilibrium

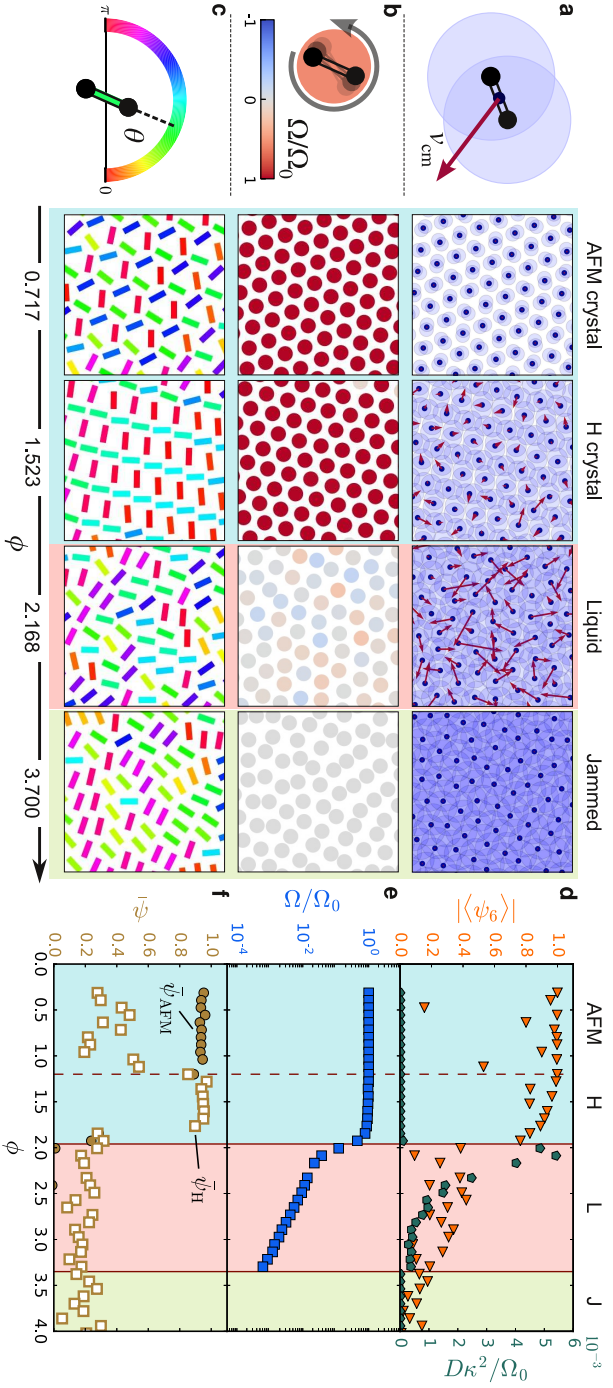


**Figure 3.2: Bulk phases of the active spinner system.** The behavior of dimer positions and orientations is investigated as a function of packing fraction  $\phi$ , for constant activity level  $\alpha = 131.026$ . Each row highlights different physical quantities of the system, shown schematically and displayed for simulation snapshots for four representative values of  $\phi$  in a–c. The snapshots cover roughly 10% of the simulation area. **a:** Center-of-mass position (dark dots) and velocities (red arrows), shown along with the soft exclusion area of individual charges (translucent discs); **b:** angular rotation speed  $\Omega/\Omega_0$ ; **c:** orientation, represented by a fixed-length segment coloured by the angle made by the dimer with the  $x$  axis. Segment length does not represent actual dimer size. **d–f:** Ensemble measurements of steady-state physical quantities, as a function of  $\phi$ . **d:** bond-orientational order parameter, and diffusivity of dimer positions; **e:** average angular speed. These quantities identify three distinct phases in different density ranges: crystal (blue background), liquid (red), and jammed (green). The rotational speed abruptly drops to zero (within numerical precision) in the jammed phase. **f:** order parameters quantifying Potts antiferromagnet ( $\bar{\psi}_{AFM}$ ) and striped herringbone ( $\bar{\psi}_H$ ) order in the phase relationships between rotating dimers in the crystal.

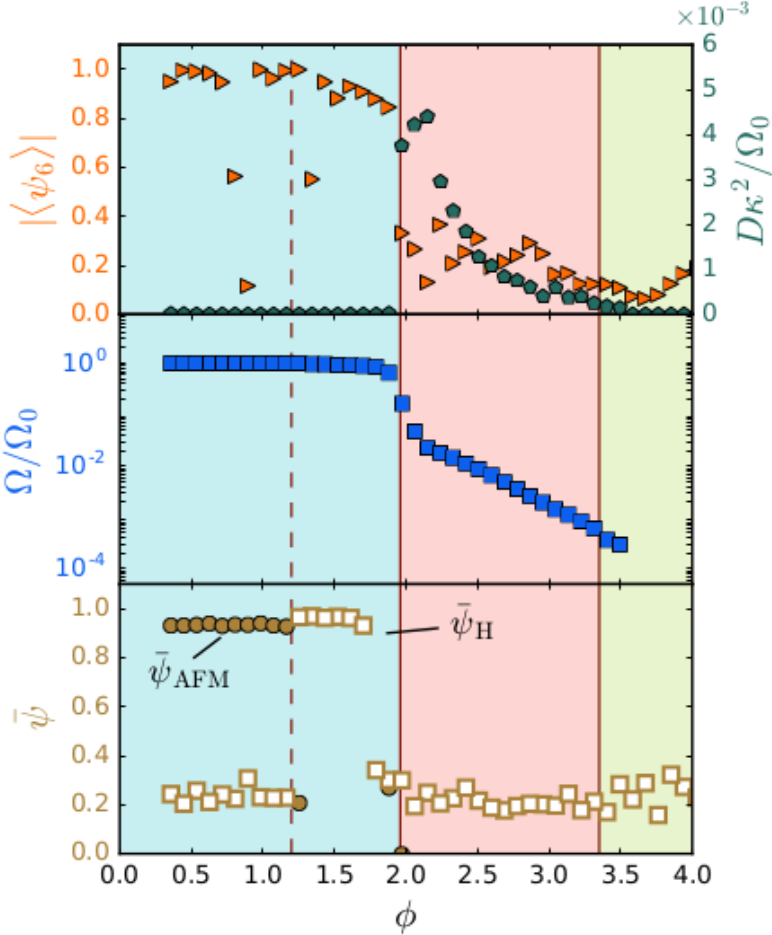


**Figure 3.3:** Ensemble measurements of steady-state physical quantities as a function of  $\phi$  for a system with  $N = 3072$  dimers, four times the system size of the simulations reported in fig. 3.2. **Top row:** bond-orientational order parameter, and diffusivity of dimer positions; **Middle row:** average angular speed. These quantities identify three distinct phases in different density ranges: crystal (blue background), liquid (red), and jammed (green). The rotational speed abruptly drops to zero (within numerical precision) in the jammed phase. **Bottom row:** order parameters quantifying Potts antiferromagnet ( $\bar{\psi}_{\text{AFM}}$ ) and striped herringbone ( $\bar{\psi}_{\text{H}}$ ) order in the phase relationships between rotating dimers in the crystal. The vertical lines are at the same values of  $\phi$  as in fig. 3.2. The density ranges for the distinct phases are almost identical for  $N = 768$  and  $N = 3072$ . The transition from liquid to jammed occurs at a slightly higher density,  $\phi_{\text{J}} \approx 3.5$  for  $N = 3072$  (compared to  $\phi_{\text{J}} \approx 3.3$  for  $N = 768$ ).



ground state of the 3-state Potts antiferromagnet (3P-AFM) on the triangular lattice [167]. When  $\phi > \phi_{C_3-C_2} \approx 1.2$ , the rotational symmetry of the pattern changes from  $C_3$  to  $C_2$  as stripes of alternating  $\delta_i \in \{0, \pi/2\}$  form along a spontaneously-chosen lattice direction fig. 3.2 c [second panel]. This phase is a dynamical analogue of the striped herringbone (H) phase observed in lattices of elongated molecules [164]. Local order parameters  $\psi_{\text{AFM}}$  and  $\psi_{\text{H}}$ , defined in section 3.1.3, measure the extent to which phase differences among neighbouring dimers match those prescribed by the respective ordered states. As shown in fig. 3.2 f, the 3P-AFM and H states are each observed over a range of densities.

To understand the origin of the phase-locked patterns, we study a minimal model of the dimer–dimer interactions. To lowest order in dimer size  $d$ , each dimer is a superposition of a charge monopole and a charge quadrupole. The monopole repulsion arranges the dimer centers into a triangular crystal with lattice constant  $a \sim 1/\sqrt{\phi}$ . We assume that the dimer positions are thus fixed and focus on the orientation dynamics, (3.2), due to the quadrupolar interactions. When averaged over the common rotation period  $2\pi/\Omega_0$ , (3.2) reduces to  $\partial_{\theta_i} \langle \sum_{j \neq i} \mathcal{V}(\mathbf{r}_j - \mathbf{r}_i, \theta_i, \theta_j) \rangle_t = 0$ ; i.e. the nonequilibrium steady states extremize the time-averaged potential energy as a function of orientation.

Upon ignoring fluctuations around the constant-speed evolution  $\theta_i(t) = \Omega_0 t + \delta_i$ , and considering only nearest-neighbour interactions among dimers, the average effective energy takes the compact form:

$$V_{\text{eff}} \equiv \left\langle \sum_{j \neq i} \mathcal{V}(\theta_i - \theta_j) \right\rangle_t = \sum_{\langle ij \rangle} \left[ A_1 + A_2 \left( \frac{d}{a} \right)^4 \cos 2(\delta_i - \delta_j) \right], \quad (3.3)$$

where  $A_1$  and  $A_2$  vary with density, see section 3.1.4 for details. For an infinite lattice of dimers,  $V_{\text{eff}}$  has arbitrarily many extrema. However, the extrema can be exhaustively listed for a *triangle* of neighbouring dimers. Up to a global phase shift and vertex permutations, the effective energy as a function of the phase shifts  $\{\delta_1, \delta_2, \delta_3\}$  on the triangle vertices has three unique extrema at  $\{0, \pi/3, 2\pi/3\}$ ,  $\{0, 0, \pi/2\}$ , and  $\{0, 0, 0\}$ . The 3P-AFM and H phases respectively extend the first and second of these extrema onto the infinite triangular lattice, and are thus also extremal states of the periodic crystal. In fact, the 3P-AFM state is the *global* energy minimum for  $V_{\text{eff}}$ , as seen by mapping the

effective energy to the antiferromagnetic  $XY$  model on the triangular lattice [162]<sup>♣</sup>. The extremum with phase values  $\delta_i = 0$ , which would correspond to all dimers sharing the same orientation at all times, maximizes the frustration of spinning by interactions and is not observed in our simulations.

In summary, spinning dimers are frustrated. The spatiotemporal-crystal states that are compatible with the mutual frustration of the position and orientation degrees of freedom are captured by the extrema of the effective potential  $V_{\text{eff}}$ . However, in principle, active spinner crystals could harbour a multitude of other phase-locked patterns, which cannot be reduced to repetitions of a single triangular unit but nevertheless extremize  $V_{\text{eff}}$ . These may be accessible by modifying the initial or boundary conditions, or the dynamics of approaching the nonequilibrium steady state.

### 3.1.3 Order parameters

The local bond-orientational order parameter  $\psi_{6,i} = \sum_{j=1}^{n_i} e^{6i\theta_{ij}} / n_i$ , where  $j$  indexes the  $n_i$  nearest neighbours of  $i$  and  $\theta_{ij}$  is the angle made by the bond connecting  $i$  and  $j$  with the  $x$  axis, measures the extent to which the neighbours of dimer  $i$  match the orientational order of the triangular lattice. The global order parameter  $|\langle\psi_6\rangle| = |\sum_{i=1}^N \psi_{6,i} / N|$  measures the extent to which local bond orientations are aligned across the system. A perfect triangular lattice has  $|\langle\psi_6\rangle| = 1$ .

The local order parameters  $\psi_{\text{AFM},i}$  and  $\psi_{\text{H},i}$  report whether the orientations of dimer  $i$  and its nearest neighbours  $j$  (identified via a Delaunay triangulation) are consistent with the expected phase differences for the 3P-AFM and H crystal phases respectively. To identify the 3P-AFM phase, we check whether orientation differences between neighbours are  $\pm\pi/3$ , by computing:

$$\psi_{\text{AFM},i} = \frac{1}{z_i} \sum_{j=1}^{z_i} 1 - \frac{1}{3} [4 \cos^2(\theta_{ij}) - 1]^2, \quad (3.4)$$

---

<sup>♣</sup>The effective energy inherits a discrete and a continuous ground-state degeneracy from the antiferromagnetic  $XY$  model. An arbitrary global phase shift gives the same state, but this is equivalent to a choice of  $t = 0$  in the description of the orientations. The discrete degeneracy is in the chirality of phase order ( $0 \rightarrow \pi/3 \rightarrow 2\pi/3$  vs.  $0 \rightarrow 2\pi/3 \rightarrow \pi/3$ ) upon circling a plaquette. Adjacent plaquettes always have opposite chirality, and the two possible chirality arrangements on the triangular lattice provide two distinct ground states.

where  $\theta_{ij} = \theta_i - \theta_j$  and  $z_i$  is the number of neighbours of dimer  $i$ . The expression evaluates to unity if  $[(\theta_i - \theta_j) \bmod \pi] \in \{\pi/3, 2\pi/3\}$  for all neighbours, and has an expectation value of zero if angle differences are randomly distributed.

For the H phase, we first arrange the neighbours in order of increasing angle made by the link connecting  $i$  and  $j$  with the  $x$  axis. Our goal is to evaluate the closeness of all possible circular shifts of this neighbour arrangement with the sequence  $S \equiv \{0, \pi/2, \pi/2, 0, \pi/2, \pi/2\}$ . We define the shift  $k$  as the integer in  $\{0, 1, 2\}$  which minimizes  $\sin^2(\theta_{ik}) + \sin^2(\theta_i - \theta_{k+3})$  in the ordered arrangement. The local order parameter is then computed via:

$$\psi_{\text{H},i} = -\frac{1}{z_i} \sum_{j=1}^{z_i} \cos \left( \begin{cases} 2\theta_{ij} + \pi, & \text{if } j \bmod 3 = k \\ 2\theta_{ij}, & \text{otherwise} \end{cases} \right), \quad (3.5)$$

which evaluates to unity only if the sequence of  $\theta_{ij}$  starting from  $j = k$  matches  $S$  and is close to zero for a random distribution of dimer orientations.

Under periodic boundary conditions, the crystals form phase-locked domains separated by defects and grain boundaries which bring down the value of the order parameters from unity when averaged over all points. In fig. 3.2 f, we identify the predominant local order within domains by plotting the most probable values  $\bar{\psi}_{\text{AFM}}$  and  $\bar{\psi}_{\text{H}}$ . These are obtained by binning the local values  $\psi_i$  from every 50<sup>th</sup> frame in the range  $8000 \leq p \leq 10000$  into 20 equally spaced bins, and reporting the coordinate of the bin with highest occupancy.

### 3.1.4 Effective interaction between dimer pairs

In the limit that the dimer length  $d$  is small compared to the dimer separation, each dimer can be considered a superposition of a monopole carrying the net charge  $2b$  and a quadrupole charge distribution. Therefore, the interaction between a pair of dimers can be written as a sum of monopole–monopole, monopole–quadrupole, and quadrupole–quadrupole terms. The monopole–monopole contribution is independent of dimer orientation. Suppose the angle made by dimer  $i$  evolves in time as  $\theta_i = \Omega_0 t + \delta_i$ . By symmetry considerations, the monopole–quadrupole contribution integrates to a quantity which is independent of the phases  $\delta_i$ . The quadrupole–quadrupole contribution does depend on the relative phases, and has the form

$$E_{ij} = J(r_{ij}) \cos(2\theta_i - 2\theta_j) + K(r_{ij}) \cos(2\theta_i + 2\theta_j - 4\phi_{ij}), \quad (3.6)$$

where  $\phi_{ij}$  is the angle made by the link connecting  $i$  and  $j$  with the  $x$ -axis, and  $J, K$  are functions of the center-of-mass separation  $r_{ij}$ , set by the Yukawa parameters:

$$J(r) = \frac{b}{128r} \left(\frac{d}{r}\right)^4 e^{-\kappa r} [9(1 + \kappa r) + 5(\kappa r)^2 + 2(\kappa r)^3 + (\kappa r)^4], \quad (3.7)$$

$$K(r) = \frac{b}{128r} \left(\frac{d}{r}\right)^4 e^{-\kappa r} [105(1 + \kappa r) + 45(\kappa r)^2 + 10(\kappa r)^3 + (\kappa r)^4]. \quad (3.8)$$

For the rotating dipoles with constant angular speed  $\Omega_0$  with fixed center-of-mass positions separated by the lattice spacing  $a$ , we have

$$E_{ij} = J(a) \cos(2\delta_i - 2\delta_j) + K(a) \cos(4\Omega_0 t + 2\delta_i + 2\delta_j - 4\phi_{ij}). \quad (3.9)$$

When the energy is integrated over a cycle, the second term integrates to zero, and hence the average potential energy over the cycle is  $(1/T) \int_0^T E_{ij} dt = J(a) \cos(2\delta_i - 2\delta_j)$ .

### 3.1.5 Melting and kinetic arrest

We now elucidate how synchronized spinning motion frustrates positional order and melts dense spinner crystals. As the packing fraction is increased, we observe a *loss* of crystalline ordering, signalled by a sharp drop in  $|\langle\psi_6\rangle|$  from 1 to 0.2 at  $\phi = \phi_{\text{melt}} \approx 1.9$ . This drop coincides with the onset of diffusive dynamics of the dimer centers of mass at long times. The diffusivity  $D \equiv \lim_{t \rightarrow \infty} \langle |\mathbf{r}_i(t_0 + t) - \mathbf{r}_i(t)|^2 \rangle_i / t$  is nonzero for a range of densities above  $\phi_{\text{melt}}$ , characteristic of a liquid phase. Melting is accompanied by a disruption of the phase-locked spinning dynamics, as quantified by (i) a drop in the average spin velocity to below  $0.1\Omega_0$ , fig. 3.2 e, (ii) a marked increase in spin speed fluctuations, fig. 3.4, and (iii) a loss of H order in the orientations, fig. 3.2 f. Figure 3.2 a–c (third column) shows a typical liquid configuration with no discernible order in the positions, orientations, or spinning speeds.

The melting of the dimer crystal upon increasing the density, at odds with the typical behavior of athermal or equilibrium repulsive particles, is a direct result of the orientational dependence of dimer–dimer interactions coupled with the active spinning. The monopole part of the pair interaction is responsible for the crystalline arrangement of dimer centers. The quadrupolar component generates a gearing effect, which hinders the activity-driven co-rotation of

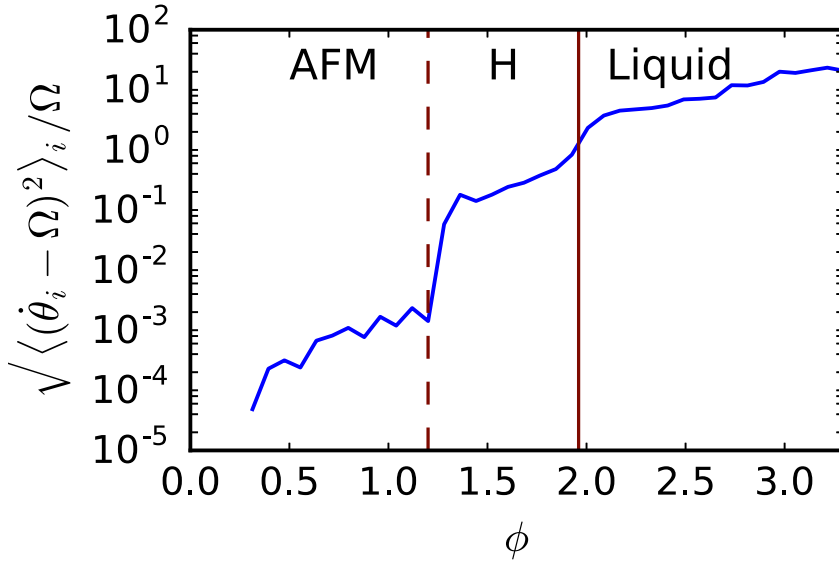


**Figure 3.4:** Fluctuations in dimer spin velocities  $\dot{\theta}_i$  around their mean value  $\Omega$  in the steady state for the simulations under periodic boundary conditions with  $\alpha = 131$ ,  $\beta = 0.0075$ . The fluctuations are quantified by the standard deviation of spin velocities, normalized by their mean. The normalized fluctuations are negligible in the 3P-AFM crystal phase ( $\phi < 1.2$ ) and small in the H crystal phase ( $1.2 < \phi < 1.9$ ). They become very large in the liquid phase ( $\phi > 1.9$ ), showing that dimers no longer rotate uniformly in the liquid; their rotational dynamics are dominated by interactions, which change constantly as dimers diffuse through the liquid. In the jammed phase ( $\phi > 3.3$ ), the mean spin velocity  $\Omega = 0$  and the normalized spread in spin velocities is undefined.

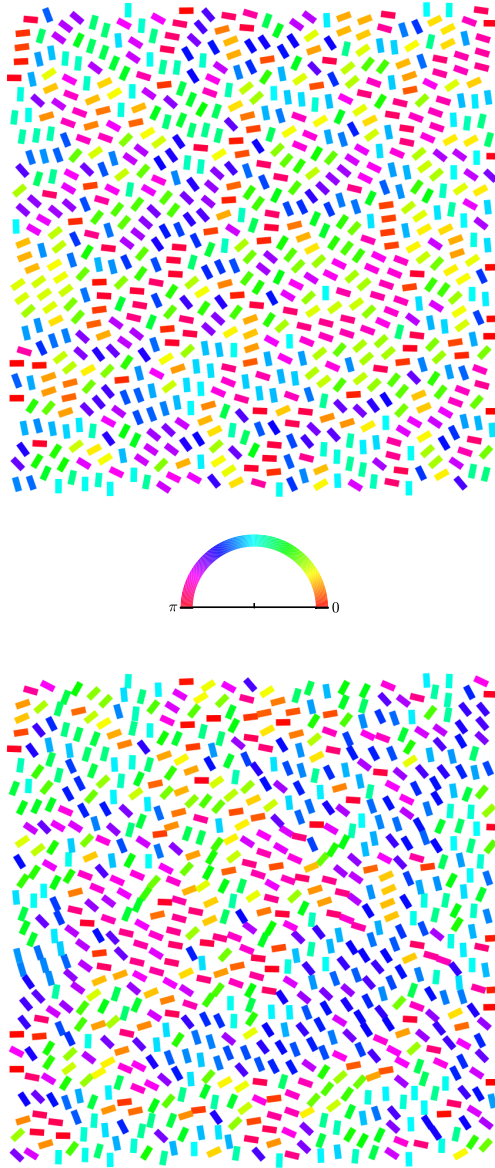


**Figure 3.5:** Snapshot of a simulation in the jammed phase ( $\alpha = 131.026$ ,  $\phi = 3.7$ ) coloured by (top) orientation angle and (bottom) orientation angle multiplied by 3. Regions of uniform colour on the right indicate regions where dimers are aligned modulo  $\pi/3$ .

adjacent dimers as shown schematically in fig. 3.2 1c. The competition between interactions and active spinning results in geometrical frustration of the crystalline order, akin to the frustration of antiferromagnetic Ising spins on the triangular lattice. Increasing the density strengthens the quadrupolar component of the interactions relative to the monopole component, *destabilizing* the crystal at the threshold packing fraction  $\phi_{\text{melt}}$ . In the liquid state, the frustration of in-place dimer rotation by interactions is partially relieved by dimers constantly sliding past each other, at the cost of crystalline and phase-locked order.

Upon increasing the packing fraction beyond  $\phi_{\text{melt}}$ , the diffusive and spinning dynamics slow down as interactions become more prominent. At  $\phi = \phi_{\text{J}} \approx 3.3$ , the diffusivity and spinning speed of the ensemble both drop abruptly to zero, signifying a sharp transition from a liquid to a frozen solid in which interactions completely overwhelm the external drive [36]. As shown by representative snapshots fig. 3.2 a–c [fourth column] and the hexagonal order parameter fig. 3.2 d, the dimer positions and orientations in the frozen state do not exhibit the ordering of the crystalline phases. However, a different form of short-range orientational order persists: dimers tend to form ribbon-like assemblies which share a common alignment, see fig. 3.2 c [fourth panel], and fig. 3.5. This structure, which locally resembles smectic ordering in liquid crystals, is a consequence of the constraints on tightly packing repulsive dimers. The full description of this state, reminiscent of a degenerate crystal [156], goes beyond the scope of our work.

### 3.2 Confinement-induced collective motion

At a microscopic level, the bulk phases are distinguished by the relative importance of rotational drive and orientation-dependent interactions. For a steady state to be attained, torques must be balanced globally as well; in a confined system, the overall torque may be balanced by viscous drag as well as boundary forces. To investigate the interplay between rotational drive, interactions, and confinement, we simulated a system confined by a circular frictionless boundary as depicted in fig. 3.6 a, for the same particle number ( $N = 768$ ), activity level and density range as in fig. 3.2. Densities are changed by varying the circle radius, since  $\phi = NA/\pi R^2$ . Figure 3.6 a shows the dimer center-of-mass motion for three representative densities across different phases, all of which display spontaneous macroscopic flows.

Measurements of the coarse-grained azimuthal velocity  $v_\theta(r)$  as a function of distance  $r$  from the disc center, see section 3.3, reveal qualitative differences in the collective flows across phases. In both the crystal ( $\phi = 0.827$ ) and frozen ( $\phi = 3.750$ ) phases, the angular velocity about the disc center,  $\omega(r) = v_\theta(r)/r$ , is constant throughout the disc fig. 3.6 b, showing that the ensemble rotates around the center in unison as a rigid body. By contrast, the angular velocity profile is nonuniform for the liquid ( $\phi = 2.395$ ), growing monotonically with distance from the disc center. These distinct behaviors persist over the entire phase diagram, as shown in fig. 3.6 c which compares the steady-state values of the flow angular velocity at the center [ $\omega(0)$ ] and edge [ $\omega(R)$ ] of the disc as a function of density. The center and edge values coincide in the solid phases, consistent with rigid-body rotation, whereas the liquid phase shows a persistent enhancement of flow at the edge. Collective vortical motion and boundary flows were previously demonstrated in suspensions of swimming cells [40, 62]. Their spatial structure and physical origin are, however, profoundly different from the confinement-induced flows reported here, which depend on the chiral activity of the spinners as we now elucidate.

### 3.2.1 Spontaneous collective rotation of rigid phases

The rigid-body rotation in the two solid phases, ordered and jammed, can be understood by balancing torques about the center of the circular boundary to obtain an acceleration-free steady state. The forces exerted by the boundary, being radially oriented, do not exert torque. Thus, the driving torques acting on the dimers must be balanced by drag forces. In the crystal interior, dimers homogeneously and steadily spin about their individual centers at a rate  $\Omega_0$ , fig. 3.6 a, and the resulting friction balances the driving torques at all times. However, the spinning of the outermost layer of  $N_e$  dimers is obstructed by the hard boundary as shown schematically in fig. 3.1 e, which implies that the driving torques on these dimers are not balanced by spinning. Rather, these torques drive an overall rotation of the crystal. The corresponding rigid-body rotation speed,  $\omega_{\text{rb}}$ , is obtained by balancing the net drive  $N_e\tau$  against the net drag torque due to the rigid-body rotation which scales as  $N\gamma\Omega R^2$ , thereby leading to  $\omega_{\text{rb}} \sim (N_e/N)\tau/\gamma R^2 \propto \phi$ .

In the frozen phase, local spinning of dimers relative to their neighbours is completely frustrated by interactions. Therefore, the entire external torque  $N\tau$  is balanced solely by the drag due to orbital motion, giving rise to  $\omega_{\text{rb}} \sim \tau/\gamma R^2 \propto \phi$ . The measured rotation speeds quantitatively match the predictions due to overall torque balance — solid and dashed lines in fig. 3.6 c.



### 3.2.2 Emergent edge current in active spinner liquids

The rigid-body motion of the two solid phases relies on the transmission of torque via shear stresses throughout the sample. If the disc is partitioned into circular annuli, the net external drive acting on each annulus differs from the net drag torque; neighboring annuli must exert shear forces on each other to balance the total torque. Unlike the solid phases, the liquid cannot support a shear stress through elastic deformations, which qualitatively explains the absence of pure rigid-body rotation, fig. 3.6 a and b. For a quantitative description of the emergent flow, we use a continuum theory of an active chiral liquid coupled to a solid substrate. This phenomenological model, introduced in Stark et al. [109] and Tsai et al. [111], generalizes the so-called micropolar-fluid hydrodynamics [66, 171] by including couplings to a frictional substrate.

Assuming incompressibility (as justified by the lack of significant spatial variations in dimer density), the hydrodynamic description relies solely on the conservation of momentum and angular momentum, and therefore involves two coarse-grained fields: the flow velocity  $\mathbf{v}(\mathbf{r})$ , and the internal angular rotation, or spin, field  $\Omega(\mathbf{r})$ . The hydrodynamic equations take on a compact form when written in terms of  $\Omega(\mathbf{r})$  and the scalar vorticity,  $\zeta(\mathbf{r}) = \frac{1}{2}\hat{\mathbf{z}} \cdot \nabla \times \mathbf{v}(\mathbf{r})$ . In the viscous steady-state limit, these equations, which respectively amount to local torque and force balance, are [109, 111]:

$$D_\Omega \nabla^2 \Omega - \Gamma^\Omega \Omega - \Gamma(\Omega - \zeta) + \rho\tau = 0, \quad (3.10)$$

$$(4\eta + \Gamma) \nabla^2 \zeta - 4\Gamma^v \zeta - \Gamma \nabla^2 \Omega = 0, \quad (3.11)$$

where  $\rho$  is the active-spinner-fluid density,  $\eta$  is the shear viscosity, and  $D_\Omega$  is a spin viscosity controlling the diffusive transport of angular momentum. The coefficients  $\Gamma^\Omega$  and  $\Gamma^v$  quantify the dissipation of angular and linear momentum respectively due to substrate friction. The crucial spin-vorticity coupling is embodied in the rolling friction  $\Gamma$ , which coarse-grains the frustration between rotations and interactions outlined in fig. 3.1 c. Orientation-dependent interactions hinder the free spinning of adjacent fluid elements, causing shear stresses proportional to  $\Gamma$  unless the elements flow past each other in such a way that the vorticity cancels the local spin.

Analysis of the hydrodynamic equations reveals that spatial variations in the local spin field induce persistent flows. In the absence of boundaries, the equations admit the flow-free solution  $\Omega = \rho\tau/(\Gamma^\Omega + \Gamma) = \Omega$ ,  $\zeta = 0$ . If a hard boundary hinders spinning, however,  $\Omega(\mathbf{r})$  varies from its value imposed by the boundary to the constant interior value  $\Omega$  over a length scale  $\lambda_\Omega =$

$[D_\Omega/(\Gamma + \Gamma_\Omega)]^{\frac{1}{2}}$  set by the competition between diffusion and dissipation of local spin. The spatial variations in  $\Omega$ , confined to the boundary, act as a source for vorticity which itself decays over a length scale  $\lambda_\zeta = [(4\eta + \Gamma)/(4\Gamma^v)]^{\frac{1}{2}}$  set by drag. These predictions match the simulation results, and a fit to radially symmetric spin and flow fields (dashed lines in fig. 3.6 b second panel) provides quantitative agreement with four fitting parameters, see section 3.2.3 for more details.

The spontaneous liquid flow only requires the obstruction of spinning by the boundary, independently of its geometry. To highlight the robustness of this emergent flow, we also study active spinner liquids in a slab geometry with two edges aligned perpendicular to the  $x$  axis and periodic boundary conditions along  $y$ , as shown in fig. 3.6 e. This geometry suppresses rigid-body rotation in all phases; excess driving torques are balanced by normal boundary forces. Accordingly, no dimer motion is measured in the crystal and jammed phases, fig. 3.6 d. However, a persistent flow parallel to the slab edges arises in the liquid phase, demonstrating that the emergence of localized shear flows at edges is a *robust* feature of geometrically confined active spinner liquids. The mechanism for the edge current is the exchange between local spin and vorticity described above, which hinges on the orientation dependence of dimer-dimer interactions. The hydrodynamic description quantitatively reproduces the flow velocity profile  $v_y(x)$  and spin field  $\Omega(x)$ , fig. 3.6 e [dashed lines].

### 3.2.3 Hydrodynamic model

In this section, we derive closed-form approximate solutions to the hydrodynamic equations, eqs. (3.10) and (3.11) of the main text, which are useful for numerical fitting to the spin and velocity profiles of the active spinner liquid under confinement. We follow Tsai et al. [111] and introduce lengths via  $\lambda_\Omega^2 = D_\Omega/(\Gamma + \Gamma_\Omega)$  and  $\lambda_\zeta^{-2} = 4\Gamma^v/(4\eta + \Gamma)$ , and unitless parameters  $p = \Gamma/(\Gamma + \Gamma_\Omega)$  and  $q = \Gamma/(4\eta + \Gamma)$ . Then the equations become:

$$(\lambda_\Omega^2 \nabla^2 - 1)\Omega + p\zeta + \tilde{\tau} = 0, \quad (3.12)$$

$$(\nabla^2 - \lambda_\zeta^{-2})\zeta - q\nabla^2\Omega = 0, \quad (3.13)$$

where  $\tilde{\tau} = \rho\tau/(\Gamma_\Omega + \Gamma) \sim \tau/(\gamma_\Omega + \Gamma/\rho)$ . In the interior of a sample, away from the edges, we expect (and observe)  $\Omega \approx \tilde{\tau} - p\zeta$ . We also observe numerically that  $p\zeta$  is negligible compared to the other two terms. Since  $\langle \Omega \rangle \ll \Omega_0$  in the liquid phase, this implies  $\Gamma \gg \Gamma_\Omega \Rightarrow p \approx 1$ . With these

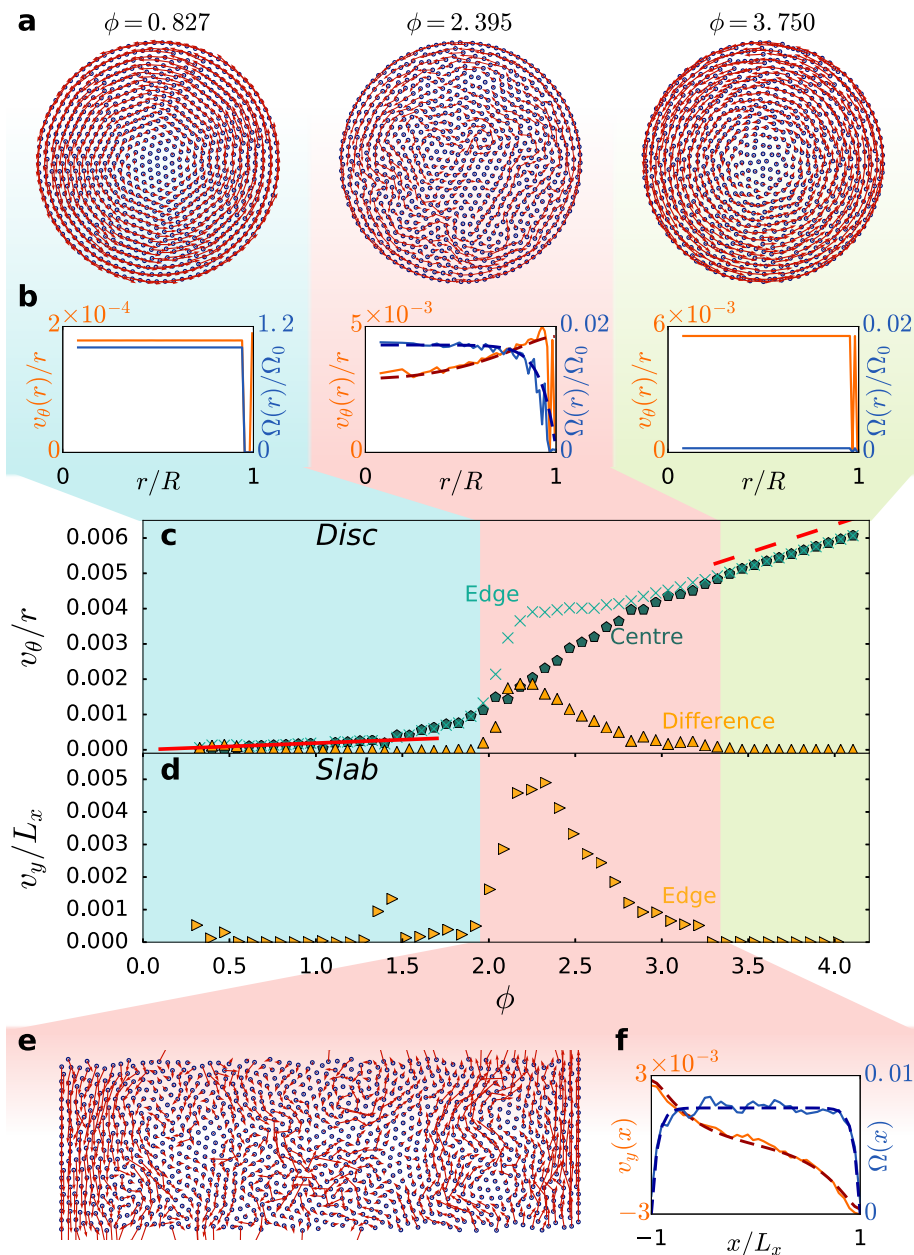
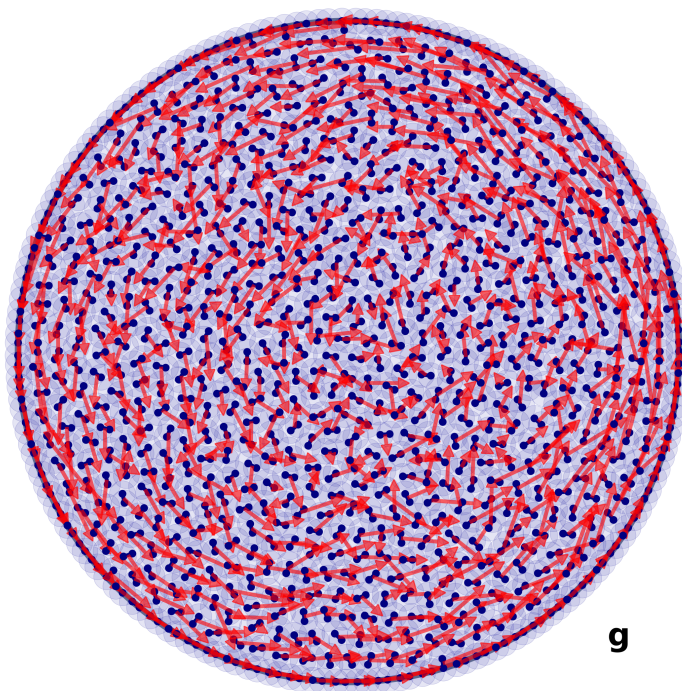


Figure 3.6: Collective motion reflects phase changes...



**Figure 3.6: Collective motion reflects phase changes.** **a**, Snapshots showing the drift of  $N = 768$  dimers confined by a circular boundary. Arrows indicate the displacements after  $\Delta t = 164/\Omega_0$  for (from left to right)  $\phi = 0.827$  (crystal),  $\phi = 2.395$  (liquid), and  $\phi = 3.750$  (jammed). Arrows are scaled differently for visibility. **b**, Time-averaged steady-state radial distributions of the orbital angular speed  $\omega(r)$  around the disc center (orange) and the local spin speed (blue), for the simulations shown in **a**. Dashed lines are fits to the hydrodynamic theory. **c**, Steady-state orbital angular speed  $\omega(r)$  in simulation units as a function of density, measured at the disc center ( $r = 0$ ) and edge ( $r = R$ ). Coincidence of the two values is consistent with rigid-body rotation. The solid and dashed red lines show the theoretical prediction for the rigid-body rotation speed in the crystal and jammed phases respectively. **d**, Steady-state tangential speed of dimers at the wall as a function of density, for  $N = 768$  dimers confined by two parallel walls perpendicular to the  $x$  direction and periodic boundary conditions along  $y$ . Density is varied by changing the area between the slabs while keeping the aspect ratio  $L_y/L_x = 2$  unchanged. **e**, Snapshot of dimer motion for 768 dimers confined between parallel slabs at  $\phi = 2.410$ , with  $L_y/L_x = 1/3$ . **f**, Averaged steady-state velocity profile between the slabs (orange) and local spin speed (blue line) for the simulation shown in **e**. Dashed lines are fits to the hydrodynamic theory. **g** Snapshots zoom in showing the drift of  $N = 768$  dimers confined by a circular boundary in the liquid phase. Arrows indicate the time averaged velocity.

simplifications, and the requirement of zero spin and zero tangential forces at the boundary, we get a closed-form solution for the two hydrodynamic fields. In the slab geometry, with slab boundaries at  $x = \pm L/2$ , they have the form:

$$\Omega(x) = \tilde{\tau} \left[ 1 - \operatorname{sech} \left( \frac{L}{2\lambda_\Omega} \right) \cosh \left( \frac{x}{\lambda_\Omega} \right) \right], \quad (3.14)$$

$$\zeta(x) = \frac{q\tilde{\tau} \left[ \operatorname{sech} \left( \frac{L}{2\lambda_\zeta} \right) \cosh \left( \frac{x}{\lambda_\zeta} \right) - \operatorname{sech} \left( \frac{L}{2\lambda_\Omega} \right) \cosh \left( \frac{x}{\lambda_\Omega} \right) \right]}{1 - \lambda_\Omega^2/\lambda_\zeta^2}. \quad (3.15)$$

The corresponding velocity field is obtained by integrating the vorticity. The current magnitude at the edges ( $x = \pm L/2$ ) is:

$$v_{\text{edge}} = \frac{2q\tilde{\tau} \left[ \lambda_\zeta \tanh \left( \frac{L}{2\lambda_\zeta} \right) - \lambda_\Omega \tanh \left( \frac{L}{2\lambda_\Omega} \right) \right]}{1 - \lambda_\Omega^2/\lambda_\zeta^2}. \quad (3.16)$$

Using these results, we can extract the values of the lengths and dimensionless parameters from the simulations. We first fit the spin field  $\Omega(x)$  since the decay length  $\lambda_\Omega$  tends to be much smaller than  $\lambda_\zeta$ , allowing the former to be fit accurately for narrow slabs where the width might be comparable to the latter. The fit to the spin field fixes the parameters  $\tilde{\tau}$  and  $\lambda_\Omega$ . The second fitting of the velocity field then fixes the remaining two parameters  $q$  and  $\lambda_\zeta$ .

The parameter values obtained from the fit for the slab simulation in main text fig. 3.6 f, with  $L = 121.43d$ , are  $\tilde{\tau} = 0.06627$ ,  $q = 0.0150$ ,  $\lambda_\Omega = 3.554d$ ,  $\lambda_\zeta = 22.65d$ . The approximation that  $p\zeta \ll \Omega$  requires  $q \ll 1$ , satisfied by the fit.

The same procedure is used for a liquid confined to a disc of radius  $R$ , for which the approximate radially symmetric solution for the spin and vorticity fields is:

$$\Omega(r) = \tilde{\tau} - \frac{\tilde{\tau}R(1-\lambda_\Omega^2/\lambda_\zeta^2)I_2\left(\frac{R}{\lambda_\zeta}\right)I_0\left(\frac{r}{\lambda_\Omega}\right)}{2b\lambda_\zeta I_1\left(\frac{R}{\lambda_\zeta}\right)I_2\left(\frac{R}{\lambda_\Omega}\right) + I_2\left(\frac{R}{\lambda_\zeta}\right)\left(R(1-\lambda_\Omega^2/\lambda_\zeta^2)I_0\left(\frac{R}{\lambda_\Omega}\right) - 2b\lambda_\Omega I_1\left(\frac{R}{\lambda_\Omega}\right)\right)}, \quad (3.17)$$

$$\zeta(r) =$$

$$\frac{bR\tilde{\tau} \left[ I_0\left(\frac{r}{\lambda_\zeta}\right)I_2\left(\frac{R}{\lambda_\Omega}\right) - I_0\left(\frac{r}{\lambda_\Omega}\right)I_2\left(\frac{R}{\lambda_\zeta}\right) \right]}{2\lambda_\zeta((b-1) + \lambda_\Omega^2/\lambda_\zeta^2)I_0\left(\frac{R}{\lambda_\Omega}\right)I_1\left(\frac{R}{\lambda_\zeta}\right) + I_0\left(\frac{R}{\lambda_\zeta}\right)\left[R(1-\lambda_\Omega^2/\lambda_\zeta^2)I_0\left(\frac{R}{\lambda_\Omega}\right) - 2b\lambda_\Omega I_1\left(\frac{R}{\lambda_\Omega}\right)\right]}. \quad (3.18)$$

Here,  $I_m$  is the modified Bessel function of first kind of order  $m$ . The parameters obtained from the fit to the approximate solution for the disc simulation in fig. 3.6 b of the main text ( $\phi = 2.395$ ,  $R = 33.65d$ ) are  $\tilde{\tau} = 0.1475$ ,  $q = 0.0161$ ,  $\lambda_\Omega = 2.484d$ ,  $\lambda_\zeta = 15.61d$ .

### 3.3 Computational methods

Our molecular dynamics simulations solve Newton's equations for a system of point particles with specified pairwise interactions, external forces, and drag coefficients. Particles interact with a pairwise repulsive Yukawa potential with identical charge  $b$  and screening length  $\kappa$ , enabled for all particle pairs with separation  $r < 10\kappa^{-1}$ . Dimers are created by connecting pairs of particles with stiff harmonic springs of equilibrium length  $d$  and spring constant  $k = 10^4 b\kappa^3$ . Torques are applied via an external force  $F = \tau/d$  oriented perpendicular to the link at all times. Each point particle also experiences a drag force proportional to velocity with coefficient  $-\gamma$ . Simulations are initialized with dimers at random positions and orientations within the simulation box. Particle positions and velocities are updated by integrating Newton's equations using a symplectic Euler method with time step  $\Delta t = 0.0086/\Omega_0$ . A typical simulation runs for  $10^7$  time steps, taking roughly 100 CPU hours for system size  $N = 768$  at the highest densities, with a snapshot of dimer data saved every  $10^3$  steps. Ensemble averages are carried out over the final 8000 snapshots.

Confining boundaries are implemented using a steep one-sided harmonic repulsive potential  $V(x) = \frac{1}{2}k_w x^2$  experienced by all particles, where  $x$  is the penetration distance into the boundary, and  $k_w = 3.14 \times 10^2 b\kappa^3$ . For simulations confined by a circular boundary, coarse-grained fields of the form  $f(r)$  are computed by dividing the simulation region into 39 concentric annuli with widths inversely proportional to their mean radius  $r$  so that the number of dimers is the same in each annulus on average. The relevant quantity averaged over all dimers occupying the annulus at  $r$  provides a discretized numerical estimate of the coarse-grained field value  $f_p(r)$  in frame  $p$ . The estimate is then averaged over the final 8000 snapshots to obtain the coarse-grained field  $f(r) = \langle f_p(r) \rangle_p$ . A similar averaging provides the coarse-grained fields  $\Omega(x)$  and  $v_y(x)$  for the slab geometry, but with the simulation area between the slabs divided into 40 strips with edges parallel to the  $y$  axis. Averaging the relevant quantity over dimers occupying a strip centered at  $x$  provides the discrete coarse-grained field value  $f_p(x)$ .

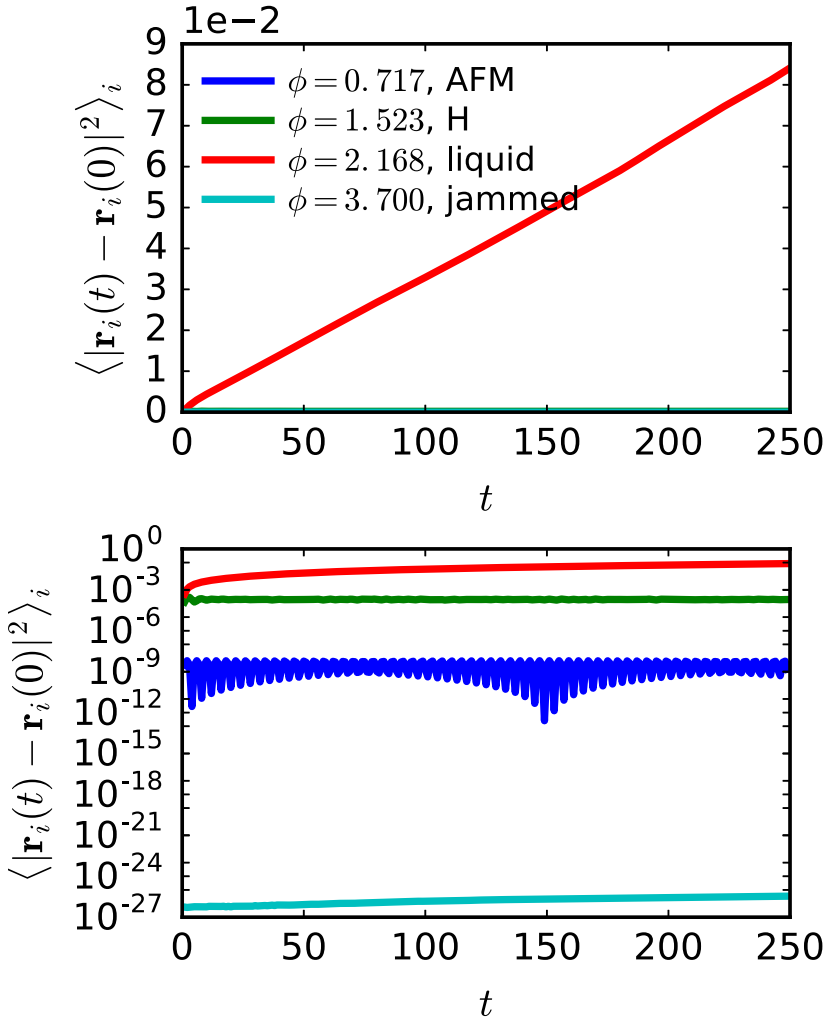


**Figure 3.7:** Mean squared displacement (MSD) of dimers over time, for the periodic system under four representative densities which are the same as in fig. 3.2. The MSD is calculated independently for 76 randomly chosen dimers (one-tenth of the total) and averaged over them. The bottom plot shows the same data on a logarithmic scale. The system in the liquid phase ( $\phi = 2.168$ ) has diffusive dimer dynamics with the mean square displacement growing linearly with time. Dimers in the crystal ( $\phi = 0.717$  and  $\phi = 1.523$ ) and jammed ( $\phi = 3.700$ ) states do not diffuse over long times. However, in the crystal phases there is a finite displacement at short times reflecting the vibrations of the dimers around their mean positions which are fixed over time. These vibrations are larger in the H phase compared to the AFM phase.

### 3.4 Conclusion

Combining numerical simulations and analytical theory, we have elucidated the phase behavior of interacting active spinners. The mutual frustration of positional and time-periodic orientational order has been shown to yield a variety of crystal and disordered phases. Although we have focused on the density dependence of the bulk and edge phenomena, the phases and their associated emergent flows persist over a broad range of activity strengths, see fig. 3.8, which makes experimental realizations feasible. Colloidal dumbbells [58, 121] spun by phoretic stresses [3] or Quincke rotation [43] would provide a near-literal realization of our model. More broadly, the essential ingredients of active spinners with orientation-dependent repulsive interactions are present in a wide variety of experimental systems including chiral liquid crystals confined to a monolayer and driven via the Lehmann effect [54], rotating nanorods propelled by biomolecular motors [134], and light-driven micromotors [15]. We also envision macroscopic realizations using chiral particles driven by airflow [35] or vibrations [111], with soft interactions provided by electrostatic or magnetic repulsion. Besides opening up new avenues to explore nonequilibrium physics in simple settings, the novel phases arising from the interplay between interactions and spinning may be exploited for tunable torque transmission [29] or for self-assembly of anisotropic particles into ordered patterns.



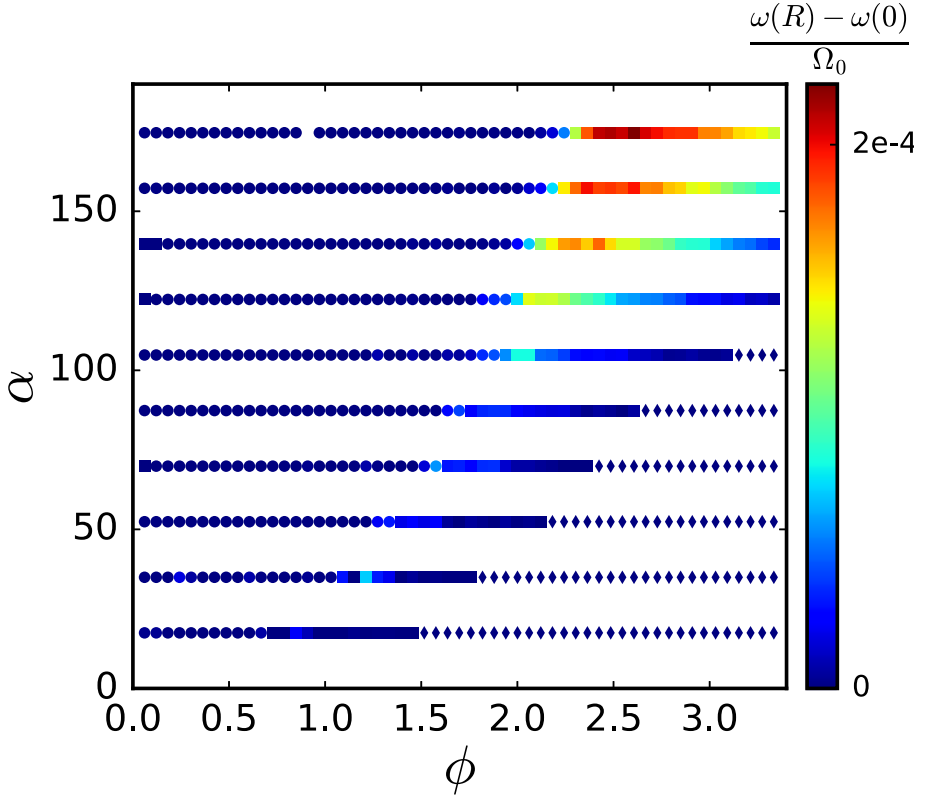


**Figure 3.8: Bulk phases are reflected in edge currents and persist over a range of torques.** The flow at the edge plotted as a function of activity level  $\alpha$  and packing fraction  $\phi$  in the disc geometry. In these simulations, the disc radius  $R = 48.27d$  was kept constant and the density was varied by changing the number of dimers confined to the disc. The tangential flow velocity  $v_\theta(r)$  was measured as for the systems in main text fig. 3.6, and the edge flow is reported as the difference in  $\omega(r) = v_\theta(r)/r$  at the edge and center of the disc. Symbols are coloured by edge current magnitude, whereas symbol shapes are chosen by values of bulk properties that identify the different phases. **Circles**, Active rotator crystals, identified by  $\langle \Omega \rangle > 0.4$  and  $\langle \psi_6 \rangle > 0.45$ . **Diamonds**, Frozen phase, identified by  $\langle \Omega \rangle < 10^{-5}$ . **Squares**, Dynamic and disordered liquid-like states, that do not satisfy the previous criteria for the crystal and frozen phases.